

# METHANE ENHANCEMENT RATIOS OVER TORONTO

by

Jon-Paul Mastrogiacomo

A report submitted in conformity with the requirements  
for the degree of Master of Science  
Department of Physics  
University of Toronto

© Copyright 2022 by Jon-Paul Mastrogiacomo

# Contents

<b>List of Figures</b>	<b>3</b>
<b>List of Tables</b>	<b>3</b>
<b>1 Introduction</b>	<b>4</b>
<b>2 Data Products</b>	<b>6</b>
2.1 TROPOMI . . . . .	6
2.1.1 CH <sub>4</sub> and CO . . . . .	6
2.1.2 NO <sub>2</sub> . . . . .	8
2.2 Cities . . . . .	9
<b>3 Methods</b>	<b>10</b>
3.1 Rotation . . . . .	10
3.2 Oversampling . . . . .	11
3.3 Angle Optimization . . . . .	11
3.4 Albedo Bias Correction . . . . .	15
3.5 Enhancement Ratios . . . . .	19
<b>4 Results and Discussion</b>	<b>21</b>
4.1 CH <sub>4</sub> :CO . . . . .	22
4.2 CH <sub>4</sub> :NO <sub>2</sub> . . . . .	24
<b>5 Future Work</b>	<b>25</b>
<b>6 References</b>	<b>27</b>
<b>A Appendix</b>	<b>34</b>
A.1 Averaging Kernels . . . . .	34
A.2 CH <sub>4</sub> :CO Examples . . . . .	35
A.3 CH <sub>4</sub> :NO <sub>2</sub> Examples . . . . .	37

## List of Figures

1	Comparison of WFMD and Operational products. . . . .	8
2	TROPOMI CH <sub>4</sub> before and after rotation. Arrow depicts wind direction. . . . .	10
3	Rotated/oversampled TROPOMI NO <sub>2</sub> omitting (left) and including (right) wind optimization. . . . .	13
4	Oversampled TROPOMI CH <sub>4</sub> with various rotation strategies. . .	14
5	Rotated/oversampled TROPOMI CH <sub>4</sub> and CO omitting (left) and including (right) wind optimization. . . . .	15
6	Rotated/oversampled CH <sub>4</sub> and apparent albedo at 2313 nm. . . .	16
7	Oversampled apparent albedo and Google Earth snapshot. . . .	17
8	Oversampled CH <sub>4</sub> (top), CO (bottom) and apparent albedo with urban areas and water removed. . . . .	18
9	OLS regression on oversampled CH <sub>4</sub> /CO against apparent albedo. Points are coloured by density. . . . .	19
10	Rotated/oversampled TROPOMI CH <sub>4</sub> and CO omitting (left) and including (right) bias correction. . . . .	20
11	CO anomalies for summer 2019. . . . .	21
12	Seasonal enhancement ratios with best correlation coefficient. . .	23
13	CH <sub>4</sub> :CO and CH <sub>4</sub> :NO <sub>2</sub> annual trends. . . . .	24

## List of Tables

1	Toronto Enhancement Ratios. . . . .	22
---	-------------------------------------	----

# 1 Introduction

Methane ( $\text{CH}_4$ ) is the second most important greenhouse gas with 32 times the warming potential of carbon dioxide over a 100-year period (Etminan et al., 2016). In the short term ( $\sim 20$  years) the radiative forcing by methane is even more severe, with 86 times the warming potential (Environment and Climate Change Canada, 2022). Due to its large effect on the climate and high fugitive emission rate, governments around the world are drafting policy and committing resources to reduce anthropogenic emissions of methane. For example, Canada has recently released a plan to reduce 75% of its methane emissions by 2030 (Environment and Climate Change Canada, 2022). But evaluating the progress of this plan depends directly on our ability to measure methane emissions. Official accounting is done with emission inventories. These are typically gridded databases of greenhouse gas emission quantities and source types, created with bottom-up methods. They are based on complex calculations incorporating information like socio-economic activity, population density, and fugitive emissions (Crippa et al., 2018; Mostafavi Pak et al., 2021). But methane emissions in particular are known to be highly uncertain in the major inventories (Saunois et al., 2020). In fact, studies in some cities have shown bottom-up estimates to be lower than direct measurements by a factor of 2 or more (Plant et al., 2019).

Atmospheric measurements and top-down approaches have been used in the past to refine and validate emission inventories (Duren and Miller, 2012) and enhancement ratios have been shown to be useful for this exact purpose. They are tracer:tracer ratios which give information about the concentration of one trace gas in terms of another. Common gases included in literature on enhancement ratios include carbon monoxide ( $\text{CO}$ ), nitrogen dioxide ( $\text{NO}_2$ ), and nitrous oxide ( $\text{N}_2\text{O}$ ). To find these ratios, an enhancement must first be identified for each relevant species. This is a part of the atmosphere with a high concentration of the trace gas from nearby emissions. Then a background concentration is calculated from surrounding data and subtracted from the whole scene to find anomalies. Finally anomalies for two different species are compared to derive enhancement ratios such as  $\text{CH}_4:\text{CO}$  or  $\text{CO}_2:\text{NO}_2$ . Akagi et al. (2011) derived enhancement ratios from in situ measurements of biomass burning and used them to improve inventory emission factors. Wunch et al. (2009) used a ground-based remote sensing instrument to measure ratios of  $\text{CO}_2$ ,  $\text{CO}$ ,  $\text{CH}_4$  and  $\text{N}_2\text{O}$  in the Californian South Coast air Basin (SCB). Then Wunch et al. (2016) used similar methods to derive ethane:methane ratios and quantify natural gas leakage in the SCB. Hedelius et al. (2018) incorporated ground and satellite measurements into a Lagrangian particle dispersion model to further improve SCB enhancement ratios.

Several studies using the tracer:tracer technique have been published based on satellite data collected from the TROPospheric Monitoring Instrument (TROPOMI, Veefkind et al., 2012). This instrument has unprecedented spatiotemporal resolution, is sensitive to tropospheric concentrations, and measures several trace gases of interest including CO, CH<sub>4</sub>, NO<sub>2</sub>, SO<sub>2</sub>, and HCHO. For example, Lama et al. (2020) used TROPOMI measurements to calculate NO<sub>2</sub>:CO ratios and investigate burning efficiencies in megacities. Plant et al. (2022) quantified CH<sub>4</sub>:CO on individual days in several cities across North America. They also validated the satellite-derived ratios with in situ aircraft measurements and inventory driven transport models. A study in review by MacDonald et al. (2022) calculates TROPOMI derived CO:NO<sub>2</sub> ratios with a similar technique, but also includes CO:CO<sub>2</sub> and NO<sub>2</sub>:CO<sub>2</sub> ratios based on CO<sub>2</sub> data from the Orbiting Carbon Observatory 2/3 (Crisp et al., 2004; Eldering et al., 2019).

One of the main advantages of the enhancement ratio technique is that it provides insight into atmospheric trace gases with an easy to understand, data-driven approach. Many studies use satellite measurements and transport model simulations to infer emissions from urban areas (Zheng et al., 2019). These are powerful tools, but they require specific expertise to set up and are computationally expensive to run. The methodology established by Plant et al. (2022) and MacDonald et al. (2022) could be used to monitor every major city in the world and calculate enhancement ratios in near real-time. However, some of the relevant trace gases are notoriously difficult to measure by satellite and the data throughput is usually poor. The previous two studies can calculate accurate enhancement ratios on days when the coverage is good, but most cities only get a handful of such days per year. For example it would be difficult to gain insight into seasonal trends with these techniques. Urban consumption of fossil fuels (CH<sub>4</sub> especially) tends to vary throughout the year, so seasonal trends are of particular interest.

Our method combines many TROPOMI overpasses together into a single scene, to try to calculate enhancement ratios for each calendar season. We use a combined rotation and oversampling technique (Fioletov et al., 2011, 2013; McLinden et al., 2012) to boost the signal of trace gas emissions above the background noise. Even when TROPOMI coverage is very good, the precision, accuracy, and footprint size of the instrument makes it difficult to observe a distinct plume or see a clear enhancement. For example, the diffuse enhancements of CH<sub>4</sub> over Toronto in single overpasses are typically ~1% above the background. But the bias and random error are reported as ~0.2% and ~0.8%, respectively (Schneising et al., 2019). We could naively average the overpasses in a given time period, but that is still not good enough. The winds around any urban area can change direction and speed, so averaging in this way would smear the plumes over a large area.

For our analysis, we need a significant enhancement that will stand out against the noisy background. To solve this problem, we rotate the overpasses according to the winds at the time of measurement to align the upwind-downwind directions. This ensures the trace gas emissions are all in roughly the same location downwind of the city. This creates a well defined plume in aggregate from overpasses that each likely had poorly resolved plumes. In addition it will average many upwind footprints, creating a smoother background for our analysis. This technique was first developed to study SO<sub>2</sub> emissions and air quality, but it has since been used for many applications. Pommier et al. (2013) used it to investigate CO emissions from megacities and Clarisse et al. (2019) used an extension to find NH<sub>3</sub> point sources. Maasakkers et al. (2022) estimated methane emissions from landfills, in part using rotated TROPOMI CH<sub>4</sub> overpasses.

## 2 Data Products

### 2.1 TROPOMI

To calculate enhancement ratios, we use measurements of CH<sub>4</sub>, CO, and NO<sub>2</sub> from the TROPOMI satellite instrument. It is a push-broom, nadir-viewing spectrometer on board the Sentinel-5 Precursor (S5P) satellite (Veefkind et al., 2012). S5P was developed by the European Space Agency (ESA) as part of the Copernicus earth observation programme. It was launched in October 2017 into a sun-synchronous orbit with a local equator crossing time of about 13:30. The main advantage of the TROPOMI instrument is its unprecedented spatiotemporal resolution. The 2600km swath width at nadir allows for global daily (or better) coverage.

#### 2.1.1 CH<sub>4</sub> and CO

We use version 1.8 of the data product from Schneising et al. (2019) as our source of CH<sub>4</sub> and CO measurements. The algorithm behind this product retrieves CH<sub>4</sub> and CO simultaneously from two fitting windows in the TROPOMI Shortwave Infrared (SWIR) band (2300-2343 nm). It is known as the Weighting Function Modified Differential Optical Absorption Spectroscopy (WFM-DOAS or WFMD) algorithm and uses a linear least-squares method to scale preselected atmospheric vertical profiles. We work directly with the column-averaged dry air mole fractions  $X_{\text{CH}_4}$  and  $X_{\text{CO}}$  provided in the data product, along with their respective uncertainties and averaging kernels. The retrieved footprints are approximately  $5.5 \times 7 \text{ km}^2$ , but considerably larger ( $7 \times 7 \text{ km}^2$ ) if measured before 6 August 2019.

The data files provided by Schneising et al. (2019) are binned by calendar day. But due to the frequent revisit rate of TROPOMI, two overpasses can be contained in a single file with different orbit numbers. When these consecutive overpasses occur, they are almost exactly 1 hour and 40 minutes apart. Since the wind direction can change in this time, we split the files based on orbit number before processing. We also filter out pixels with `xch4_quality_flag=1` and `xco_quality_flag=1` as recommended in the documentation.

We opted to use the WFMD product instead of the operational CH<sub>4</sub> (Hu et al., 2016) and CO (Landgraf et al., 2016) products primarily due to the increased CH<sub>4</sub> coverage as noted in Schneising et al. (2019). This is likely due to differences in quality filtering and in the treatment clouds and aerosols. The increased WFMD coverage can be seen directly by observing an individual overpasses. Figure 1 is a typical overpass where the CH<sub>4</sub> coverage is improved dramatically and includes footprints over the relevant city. While the CO coverage suffers slightly, preliminary testing shows that enhancements are better correlated with this increase in CH<sub>4</sub> data throughput. Schneising et al. (2019) noted the WFMD algorithm requires a clear sky for the simultaneous retrieval while the operational CO retrieval is designed to handle some cloudy scenes. This likely explains the decrease in CO coverage observed in Figure 1.

While CH<sub>4</sub> coverage improves significantly in the WFMD product, the data quality does not appear to suffer. Validation against the Total Carbon Column Observing Network (TCCON) shows that the systematic (4.24 ppb/ $\sim 0.2\%$ ) and random (12.39 ppb/ $\sim 0.8\%$ ) error are well within the quality requirements (1.5% and 1.0%) outlined by the ESA (ESA, 2017; Schneising, 2022). While a ground-based validation study for the current operational data product has not been published, Schneising et al. (2019) have compared it to their WFMD product. For example in June 2018, the two datasets had a global mean bias of 0.1%, a standard deviation of 0.7%, and a correlation coefficient of 0.85. The case for WFMD CO is similar with TCCON-derived systematic (2.62 ppb/ $\sim 2.1\%$ ) and random (5.08 ppb/ $\sim 5.8\%$ ) error significantly less than the requirements (10% and 15%). The agreement ( $R=0.99$ ) between the WFMD and operational products is much better for CO with 1.0% mean bias and standard deviation on the order of the noise level. Note that version 2 of the operational CH<sub>4</sub> and CO products being released soon improve on the WFMD error statistics. This in part motivates our plan to redo our analysis with these new products (see section 5).

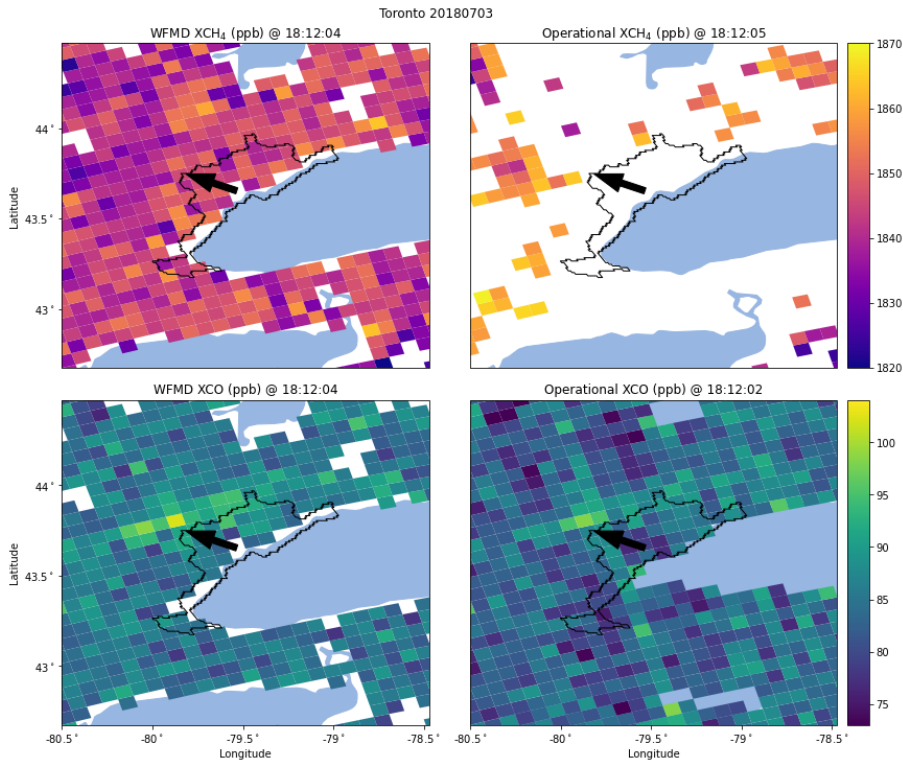


Figure 1: Comparison of WFMD and Operational products.

### 2.1.2 $\text{NO}_2$

Tropospheric vertical column densities of  $\text{NO}_2$  are calculated from TROPOMI UV-Vis measurements in the 0.405–0.465  $\mu\text{m}$  band (van Geffen et al., 2020). The  $\text{NO}_2$  footprints are approximately  $3.5 \times 5.5 \text{ km}^2$  which are notably smaller than those of the previous species. The throughput is also significantly better, with far fewer lost pixels due to clouds and aerosols. Instead of the operational  $\text{NO}_2$  product (Eskes et al., 2019), we use an intermediate reprocessing explained in Eskes et al. (2021). We chose this new dataset due to a change in the operational  $\text{NO}_2$  processor in December 2020. This reprocessing was designed to establish a consistent timeline of  $\text{NO}_2$  measurements to support research on the impact of COVID lockdowns on air quality. We filter out any pixels with  $\text{qa\_value} \leq 0.75$  as recommended in the documentation.

The  $\text{NO}_2$  data files only contain tropospheric column concentrations (molecules  $\text{cm}^{-2}$ ) and must be converted to tropospheric column-averaged dry air mole fractions (ppb). We follow Wunch et al. (2016) by dividing the column concentrations

by the dry air column,

$$X_{\text{NO}_2} = \frac{\text{column}_{\text{NO}_2}}{\text{column}_{\text{air}}^{\text{dry}}}. \quad (1)$$

And we use the following to calculate the column of dry air,

$$\text{column}_{\text{air}}^{\text{dry}} = \frac{P_s}{\{g\}_{\text{air}} m_{\text{air}}^{\text{dry}}} - \text{column}_{\text{H}_2\text{O}} \frac{m_{\text{H}_2\text{O}}}{m_{\text{air}}^{\text{dry}}}, \quad (2)$$

where  $P_s$  is the surface pressure,  $\{g\}_{\text{air}}$  is the column-averaged gravitational acceleration,  $m_{\text{air}}^{\text{dry}}$  is the molecular mass of dry air ( $28.9646 \text{ g mol}^{-1}$ ), and  $m_{\text{H}_2\text{O}}$  is the molecular mass of water ( $18.01528 \text{ g mol}^{-1}$ ). We take both the surface pressure and surface altitude from the algorithm input data contained in the TROPOMI NO<sub>2</sub> files, the latter of which is needed to calculate  $\{g\}_{\text{air}}$ . Finally, the files contain the water slant column density rather than the tropospheric water column. So to find  $\text{column}_{\text{H}_2\text{O}}$  we divide the water slant column by the tropospheric air mass factor.

We also need averaging kernels to compare NO<sub>2</sub> measurements with those of other species. To derive tropospheric versions of the total column averaging kernels we follow the process in Eskes et al. (2019). This is done by ignoring the averaging kernel above the tropopause and scaling by the air mass factors,

$$A^{\text{trop}} = \frac{M}{M^{\text{trop}}} A, \quad \text{layer} \leq \text{tropopause}, \quad (3)$$

$$A^{\text{trop}} = 0, \quad \text{layer} > \text{tropopause}, \quad (4)$$

where  $M$  and  $M^{\text{trop}}$  are the total and tropospheric air mass factors, respectively.

## 2.2 Cities

We define the extent of cities using the European Commission Joint Research Centre's (EC-JRC) Global Human Settlement layer Urban Centres Database (GHS-UCDB, Florczyk et al., 2019). The boundaries of each city are provided by a multipolygon on a  $1\text{km} \times 1\text{km}$  grid. We calculate the centroid of the city based on this multipolygon and rotate the satellite pixels about this point.

In section 3.4, we calculate an albedo correction in the Toronto area. To do this we need information about bodies of water and smaller cities in the surrounding area. We use the free vector and raster map data at [naturalearthdata.com](http://naturalearthdata.com). Specifically, we use the Urban Areas dataset at 10m resolution to identify smaller cities and towns surrounding Toronto. We also use the 10m North America Lakes dataset to include the many small lakes and rivers in the larger area.

## 3 Methods

### 3.1 Rotation

In our analysis, we work with any satellite pixels within a bounding box of the relevant city, defined by a  $0.5^\circ$  buffer from the GHS-UCDB city multipolygon. If an overpass is determined to have pixels in our working domain, we assign the overpass a wind direction which we derive from the Modern-Era Retrospective analysis for Research and Applications Version 2 (MERRA-2, Gelaro et al., 2017). This dataset has  $0.5^\circ$  latitude  $\times 0.625^\circ$  longitude spatial resolution and 3-hourly temporal resolution, so we interpolate to the location of the city centroid and satellite overpass time. Following MacDonald et al. (2022) we use winds at 50m to represent the boundary layer.

Once an overpass is assigned an associated wind direction, we rigidly rotate the overpass pixels about the city centroid to align the wind with the positive x-axis. This was adapted from Pommier et al. (2013) and an example can be seen in Figure 2. There is a possibility that pixels from outside our initial processing domain could be rotated into frame. For this reason we work on an extended domain with a  $0.7^\circ$  buffer until after this step.

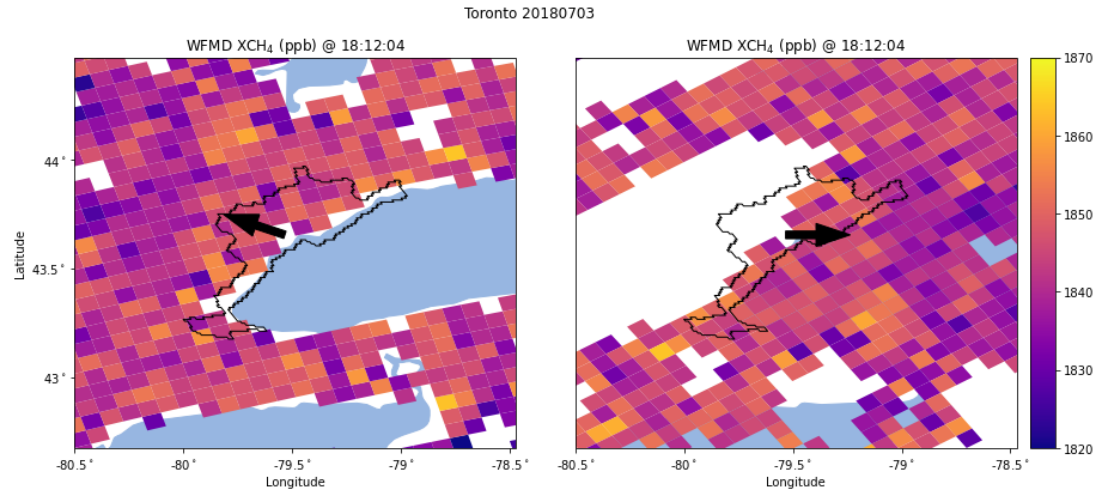


Figure 2: TROPOMI CH<sub>4</sub> before and after rotation. Arrow depicts wind direction.

### 3.2 Oversampling

For a given time period, we rotate the relevant overpasses to align the upwind-downwind directions, but the data are not in a workable form. They are in the form of irregularly shaped satellite pixels assembled in distinct overpasses. To facilitate our analysis, we want to incorporate each pixel into a single scene with data arranged on a regular grid. Overlapping upwind pixels will be intelligently averaged onto our grid reducing random noise from any one measurement and forming the background. Similarly measurements downwind will combine to form a plume with an enhancement significantly greater than the noise level in the background. In addition the plume will have a more realistic shape than can be achieved by the large rectangular pixels of the TROPOMI instrument.

This process is called oversampling and we follow Zhu et al. (2017) and Sun et al. (2018), using a  $0.01^\circ \times 0.01^\circ$  resolution grid. The contribution of each satellite measurement to a grid cell is weighted by the overlapping area, so that pixels not completely containing grid cells will have less influence. They are also inversely weighted by both the pixel observational uncertainty and pixel polygon area. The equation for oversampled grid cell  $i$  is given by

$$\bar{\Omega}(i) = \frac{\sum_{p=1}^{N(i)} \frac{A(p,i)}{S(p)\sigma(p)} \Omega(p)}{\sum_{p=1}^{N(i)} \frac{A(p,i)}{S(p)\sigma(p)}}, \quad (5)$$

where  $A$  is the overlapping area,  $S$  is the pixel area,  $\sigma$  is the reported uncertainty, and  $\Omega$  is  $X_{\text{gas}}$ . This is done for the  $N$  pixels that intersect grid cell  $i$ . Any of the ensuing geospatial figures incorporate oversampling.

### 3.3 Angle Optimization

While wind directions derived from MERRA-2 data usually give a good approximation of plume direction, there are instances in which further adjustments are necessary. In MacDonald et al. (2022) the authors apply manual adjustments to wind directions based on visual inspection of the  $\text{NO}_2$  plume. While this is a natural solution, it is an infeasible strategy for the number of overpasses we deal with in this work. Instead we follow the automated wind optimization strategy of Nassar et al. (2017, 2021). We transform latitude-longitude positions of satellite pixels into along- and cross-wind distances ( $x$  and  $y$  respectively) and simulate enhancements using a Gaussian plume model based on the following set

of equations

$$V(x, y) = \frac{F}{\sqrt{2\pi}\sigma_y(x)u} e^{-\frac{1}{2}\left(\frac{y}{\sigma_y(x)}\right)^2},$$

$$\sigma_y(x) = a \left( \frac{x + x_0}{x_c} \right)^{0.894},$$

$$x_0 = x_c \left( \frac{y_0}{a} \right)^{\frac{1}{0.894}}.$$

Here  $V$  is the vertical column downwind,  $\sigma_y(x)$  controls the width of the plume and  $F$  is the emission rate. We also have the characteristic length scale  $x_c = 1000$ , the initial width of the plume  $y_0$ , the wind speed  $u$ , and the atmospheric stability parameter  $a$  (Pasquill, 1961). We simulate the  $X_{\text{gas}}$  enhancement and use a least squares fit to scale the simulation to best match the observed TROPOMI data. Finally we calculate the correlation coefficient to determine how close our simulation is to the real measurements.

It is crucial to note that we are not making an emission estimate and we are not interested in the calculated value of  $F$ . Rather we are just interested in maximizing the correlation coefficient (which is why we frame this as an optimization problem). In Nassar et al. (2017, 2021), the authors model emissions from power plants and simulate the plume at a variety of directions to find the best fit. But in this work, we have diffuse emissions from an urban area where the observed plume is not likely to originate from a single point. So we extend the optimization in Nassar et al. (2017, 2021) to model the plume at a variety of directions and initial plume widths.

We attempt 7 evenly spaced directions with a maximum allowable adjustment of  $\pm 30^\circ$  from the MERRA-2 derived angle. And we attempt 7 evenly spaced initial plume widths between 0 and 10 km. The two angles with the best correlation coefficients are used as boundaries for a second iteration of optimization. As with the emission rate parameter, we do not use the modelled initial plume width in our analysis; its inclusion provides a better opportunity for the algorithm to find a wind direction that best aligns with the plume. The output of this algorithm for  $\text{NO}_2$  is demonstrated in Figure 3. The plume with wind direction optimization has a smaller overall area with a greater enhancement and is more closely aligned with the positive x-axis. So overall this procedure better aligns  $\text{NO}_2$  plumes from individual overpasses.

Since  $\text{NO}_2$  is short-lived and has low background concentration, some studies use the observed  $\text{NO}_2$  plume to supplement wind information from reanalysis prod-

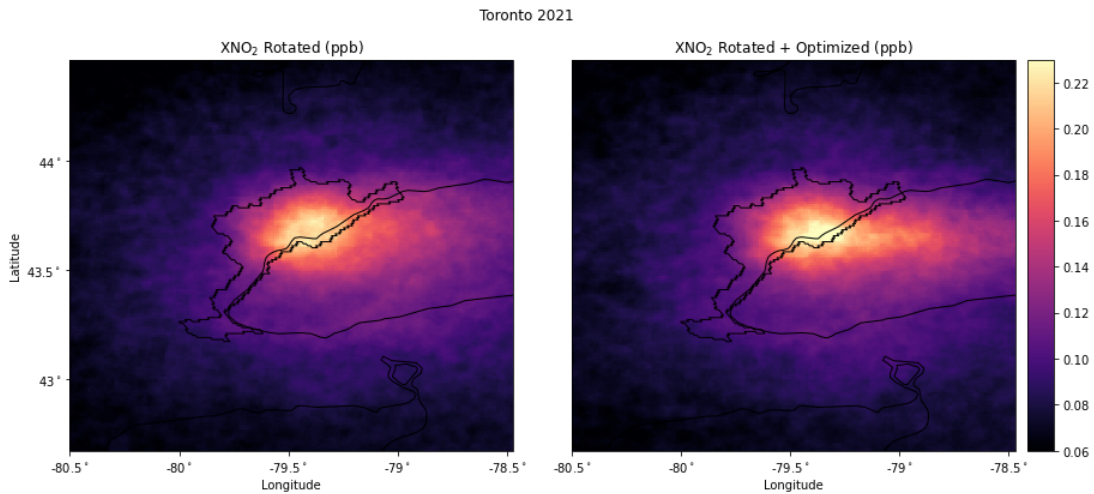


Figure 3: Rotated/oversampled TROPOMI NO<sub>2</sub> omitting (left) and including (right) wind optimization.

ucts. For example, Reuter et al. (2019) use NO<sub>2</sub> plume directions to aid in CO<sub>2</sub> emission estimates since power plants are known to co-emit NO<sub>2</sub> and CO<sub>2</sub>. In MacDonald et al. (2022) the authors also use NO<sub>2</sub> enhancements to inform the location of CO<sub>2</sub> plumes. While these species are not necessarily co-emitted by individual emission sources in cities, urban air is sufficiently well-mixed at this scale to use this approximation. We ran a series of tests using the NO<sub>2</sub> angles from our wind optimization algorithm, to inform rotation for CH<sub>4</sub> and CO overpasses. One test result for 2019 can be seen in the bottom right of Figure 4.

We also try applying this plume fitting algorithm to the CH<sub>4</sub> and CO scenes directly, but it does not improve the enhancement as dramatically as for NO<sub>2</sub>. There is an example contained in Figure 4 or we can compare the left and right sides of Figure 5. Here we see the CH<sub>4</sub> plume dose not have a greater enhancement nor is it better aligned with the positive x-axis. But the optimized CO plume might be slightly better in these two categories. The absence of dramatic improvement is likely due to two major factors. The first is the poor coverage of individual overpasses. The downwind signal usually has missing pixels (especially over water) and may not resemble a Gaussian plume, resulting in a poor maximal correlation coefficient and errant wind direction. The second factor is the relatively low enhancement. The plumes we see in CH<sub>4</sub> and CO measurements are only a few parts per billion greater than their backgrounds. This again, makes it difficult for the algorithm to confidently associate a Gaussian plume and wind direction to an overpass. In comparison, the NO<sub>2</sub> overpasses have significantly

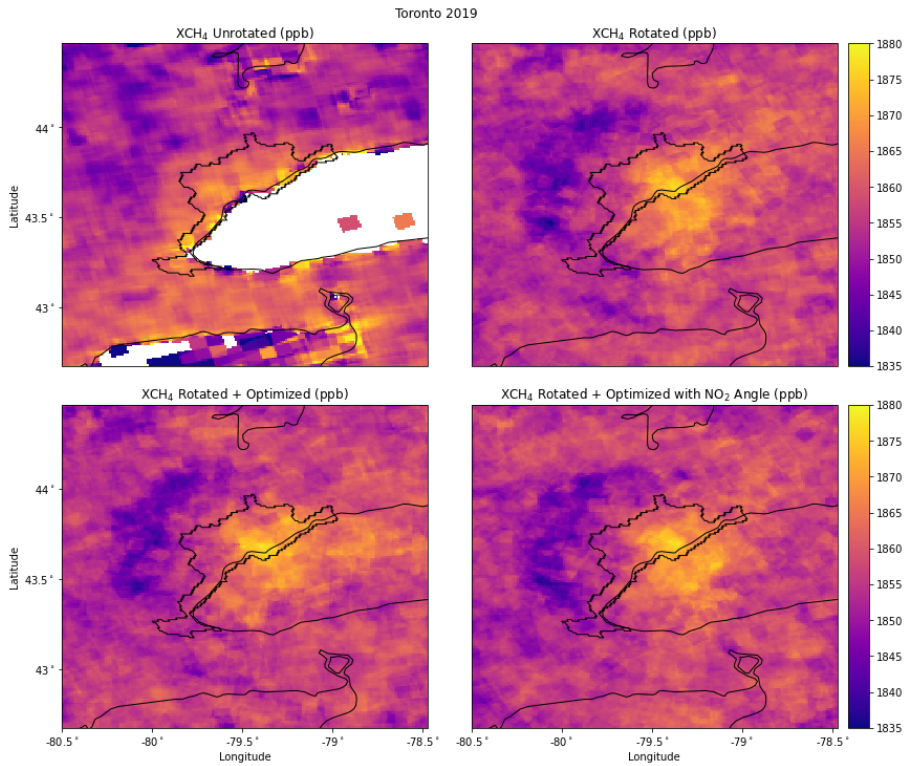


Figure 4: Oversampled TROPOMI CH<sub>4</sub> with various rotation strategies.

better coverage and significant enhancements, so the algorithm can easily associate a modelled plume to the data. Another disadvantage of optimizing the CH<sub>4</sub> and CO directly is that we would be rotating the plumes of the various trace gases by different amounts, even if they were measured at the same time. Ultimately, we use the optimized NO<sub>2</sub> angles to inform the CH<sub>4</sub> and CO rotation. A systematic analysis of the enhancement correlations could be used in the future to decide on the best optimization strategy.

One looming issue with the current implementation is that the plume always begins at the city centroid. But a city might have a plume come from an entirely different place. For example, in some overpasses over Toronto a clear NO<sub>2</sub> plume can be seen emanating from Hamilton, while the city centroid is located in the downtown core. These cases can cause the algorithm to return worse results or miss the plume entirely. A future implementation could include the starting latitude-longitude position in the optimization procedure. We could find the best plume relative to this point, translate the entire overpass to align this point with the city centroid, and rotate by the optimized angle. This would give

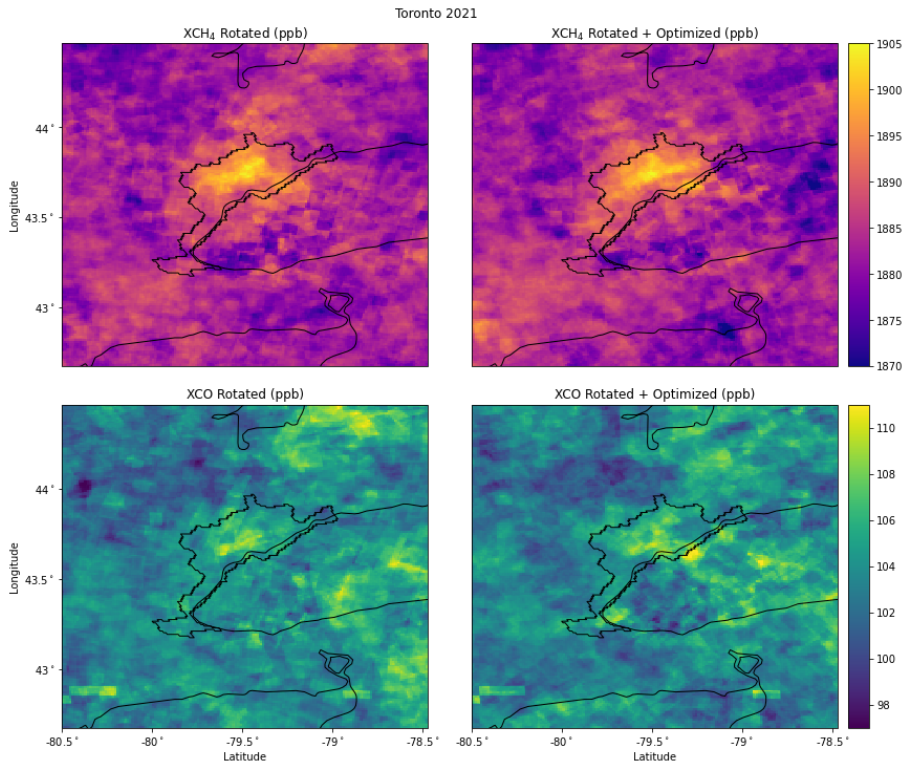


Figure 5: Rotated/oversampled TROPOMI CH<sub>4</sub> and CO omitting (left) and including (right) wind optimization.

the algorithm an even better opportunity to find the best direction and greatly increasing the alignment of individual plumes.

### 3.4 Albedo Bias Correction

While developing the methods for this work, we noticed artifacts in the upwind direction of rotated CH<sub>4</sub> data. For example in Figure 4 there is a clearly visible band of CH<sub>4</sub> grid cells that are lower than the background elsewhere. However methane is known to have a fairly consistent concentration in the troposphere, so this is overall unexpected. The main loss mechanism for CH<sub>4</sub> is due to the OH radical (Jacob, 1999), but again we do not expect high emissions of this molecule upwind of Toronto in any scenario. One possible explanation is that this low band is a feature of the retrieval algorithm or some kind of post-processing, such as a bias correction. It is not uncommon for albedo to affect space-based measurements of atmospheric trace gases, since detected sunlight is diffusely reflected by

the surface. The type of reflecting material fundamentally changes the composition of the incoming light. To be more specific, the apparent albedo reported in the WFMD product is retrieved at 2313 nm (Schneising et al., 2019). So when we refer to albedo below, we are really discussing spectral albedo in a small window around this wavelength. For example, forests have low albedo in the short-wave infrared (which includes 2313 nm) and reflects less light than would grassy fields or concrete.

We further probe this issue by rotating and oversampling all available CH<sub>4</sub> and apparent albedo data (Figure 6). We see the upwind band of low CH<sub>4</sub> even when averaging four full years of data. But the right side of Figure 6 shows a ring of low albedo surrounding the city. If an albedo bias is causing lower than expected CH<sub>4</sub> upwind, it could be suppressing a CH<sub>4</sub> plume downwind. And we could be seeing a high CH<sub>4</sub> bias over the urban area where the albedo is highest.

We also want to know what is causing the ring of low albedo around the city. Figure 7 shows a side-by-side of unrotated, oversampled albedo and a snapshot from Google Earth based on satellite imagery. The low albedo patch to the west of the city aligns with some of the densest forest in the area. It is well known that forests have lower albedo than any other relevant surface cover type like farmland, grassland, or concrete. The measurements over this western forest are being smeared into the dark ring shape we see in Figure 6. Looking more closely, we see that all of the dark patters formed from oversampled albedo data match with forested areas, as we might expect.

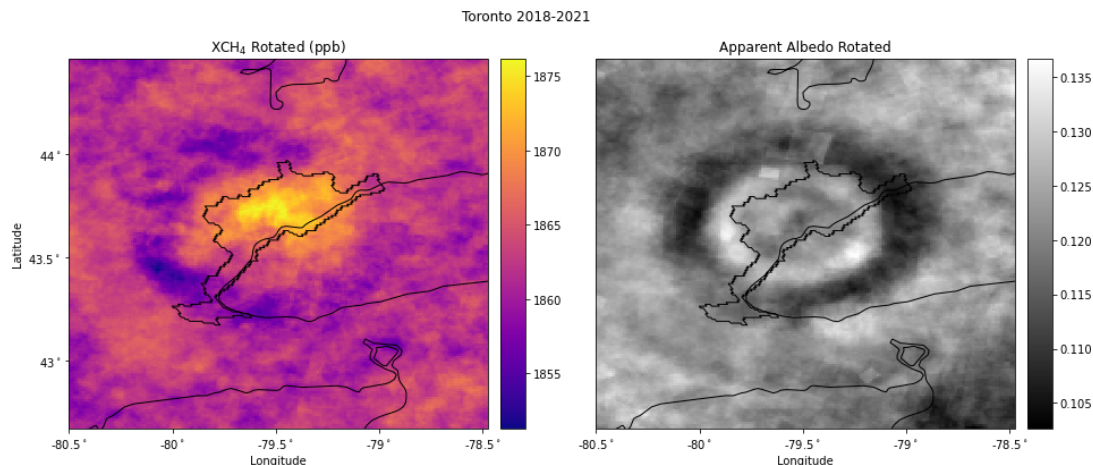


Figure 6: Rotated/oversampled CH<sub>4</sub> and apparent albedo at 2313 nm.

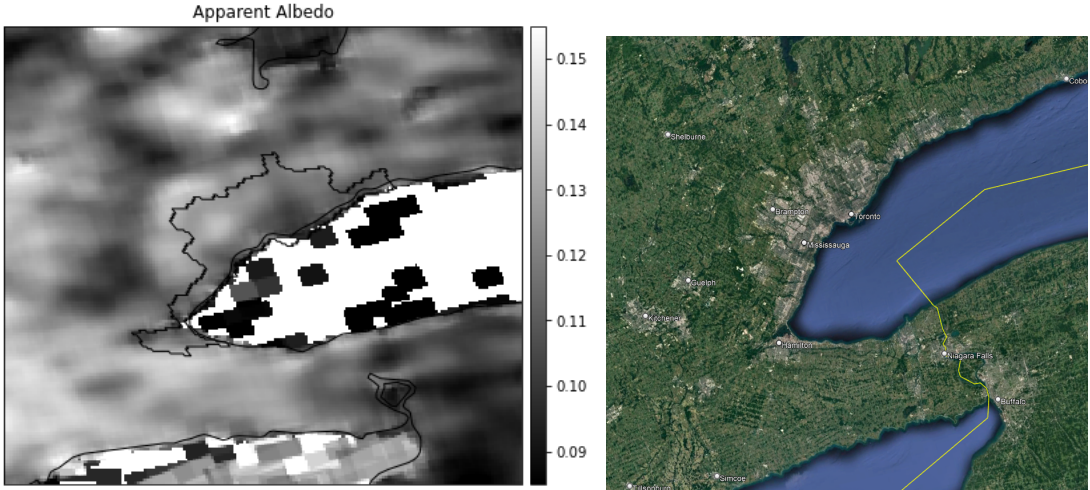


Figure 7: Oversampled apparent albedo and Google Earth snapshot.

To see if these low albedo patterns are affecting CH<sub>4</sub>, we plot all of the available column data without rotation next to the apparent albedo (top of Figure 8). We see clear bands of low albedo that are coincident with low CH<sub>4</sub>, especially north of the city. This indicates an albedo bias, possibly related to the retrieval algorithm or post-processing. In order to calculate a correction for this bias, we remove urban areas from consideration because we are trying to mitigate the influence of anthropogenic emissions on our scene and correct only for the effect of albedo. We also remove any data over water due to poor coverage. Even when we average four years of data, only a handful of pixels exist for a given grid cell over water. This gives those few pixels a disproportionately large influence on the scene and on the bias correction formula. The locations of bodies of water and surrounding urban areas are taken from [natural-earth-data.com](http://natural-earth-data.com) as latitude-longitude polygons. The polygons are buffered by 0.07° and the data is discarded; this is causing the holes seen in Figure 8.

During the development of this work, we did not notice a bias in the CO data. However, just to be sure, we plotted the unrotated CO measurements against albedo and observed the pattern that we see in methane (bottom of Figure 8). Observing a correlation with albedo in both species is important because it bolsters our argument that this is a feature of the retrieval or bias correction procedure. Note that Schneising et al. (2019) used an approach where CH<sub>4</sub> and CO are retrieved simultaneously. In the area surrounding Toronto, we do not expect the measurement patterns to match so closely for both species. There is likely not a natural co-emitting source of CO and CH<sub>4</sub>. We strongly suspect that the low

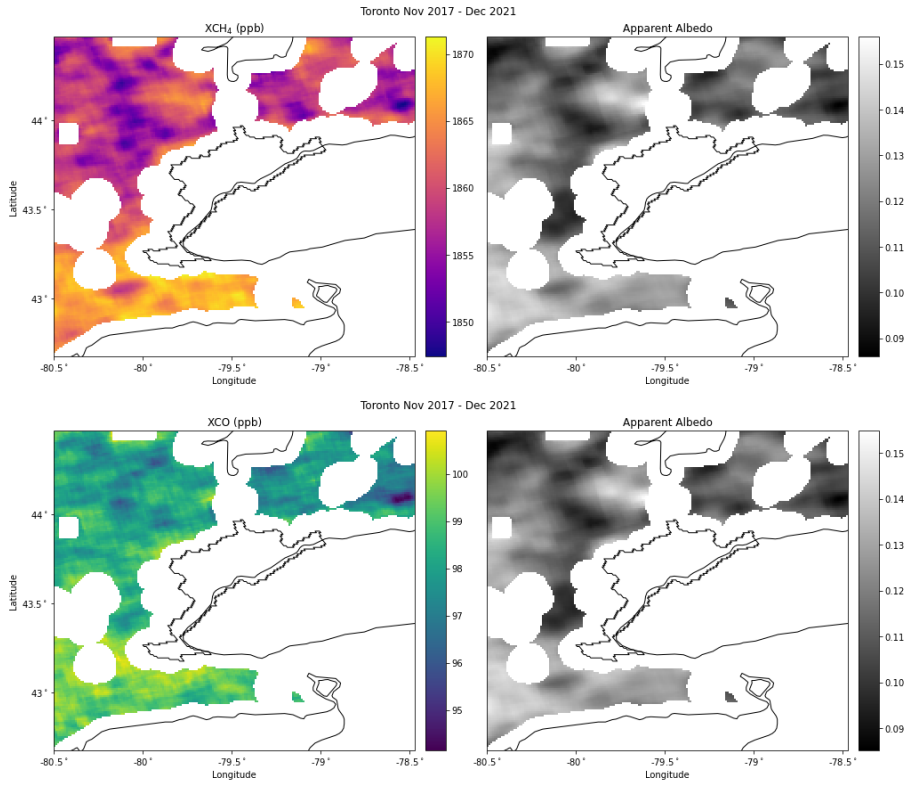


Figure 8: Oversampled  $\text{CH}_4$  (top),  $\text{CO}$  (bottom) and apparent albedo with urban areas and water removed.

albedo patterns are forested areas which are causing lower than expected column measurements. This could be further confirmed by cross referencing the albedo patterns with a satellite-based land cover data set.

To calculate the bias correction formula, we roughly follow Lorente et al. (2021), but use  $\text{CH}_4$  and  $\text{CO}$  anomalies instead of a reference value. The apparent albedo has been oversampled in the same way, as described in Section 3.2. We calculate anomalies following Section 3.5 and regress them onto the albedo values at every grid cell with Ordinary Least Squares (OLS). The regression lines can be seen in Figure 9.

The Pearson correlation coefficient for  $\text{CH}_4$  is reasonably high (0.74) and indicates good correlation between measured methane columns and albedo. To correct for this bias, we subtract the value of this line from each methane pixel before oversampling. It has the effect of increasing  $X_{\text{CH}_4}$  pixels with low albedo ( $\lesssim 0.115$ ) and decreasing those with high albedo ( $\gtrsim 0.115$ ). The correlation is slightly worse

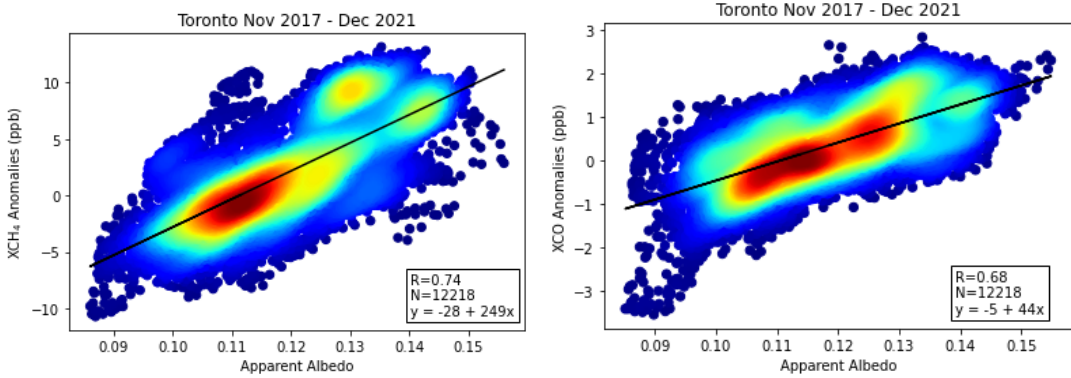


Figure 9: OLS regression on oversampled  $\text{CH}_4/\text{CO}$  against apparent albedo. Points are coloured by density.

for CO but the anomalies are still clearly dependent on albedo. Note that the line of best fit is significantly less steep for CO, and therefore the change to XCO columns will be much less significant.

Figure 10 shows the effect of the bias correction on oversampled and rotated columns in summer 2020. We see that the upwind band of low  $\text{CH}_4$  has been somewhat suppressed, but not completely eliminated. The enhancement over the city polygon has also been noticeably reduced. We do not have a good explanation for the remaining upwind low bias. Hachmeister et al. (2022) found an altitude bias in the WFMD product over Greenland. This motivated our investigation into altitude, but it showed less significant  $\text{CH}_4$  or CO correlation ( $R \approx 0.5$ ) than with albedo. And a multilinear fit of both variables showed similar correlation to that of just albedo. In some preliminary testing, both altitude corrections led to worse enhancement correlations overall, but more testing could be done to rule out their use entirely.

### 3.5 Enhancement Ratios

We follow MacDonald et al. (2022) to calculate the background for CO and  $\text{NO}_2$ . We apply a nearest neighbour fit (Altman, 1992) with a constant radius of 150km ( $1.35^\circ$ ) on the bottom 75% of the data. This fits a 2-dimensional surface to the rotated data, while avoiding the influence of anthropogenic emissions (bottom left Figure 11). On the spatial scale we are working with, we expect a constant  $\text{CH}_4$  background and do not fit a varying surface to the oversampled data. Rather we take an average of the bottom 75% of the data and use that as the background for the entire scene.

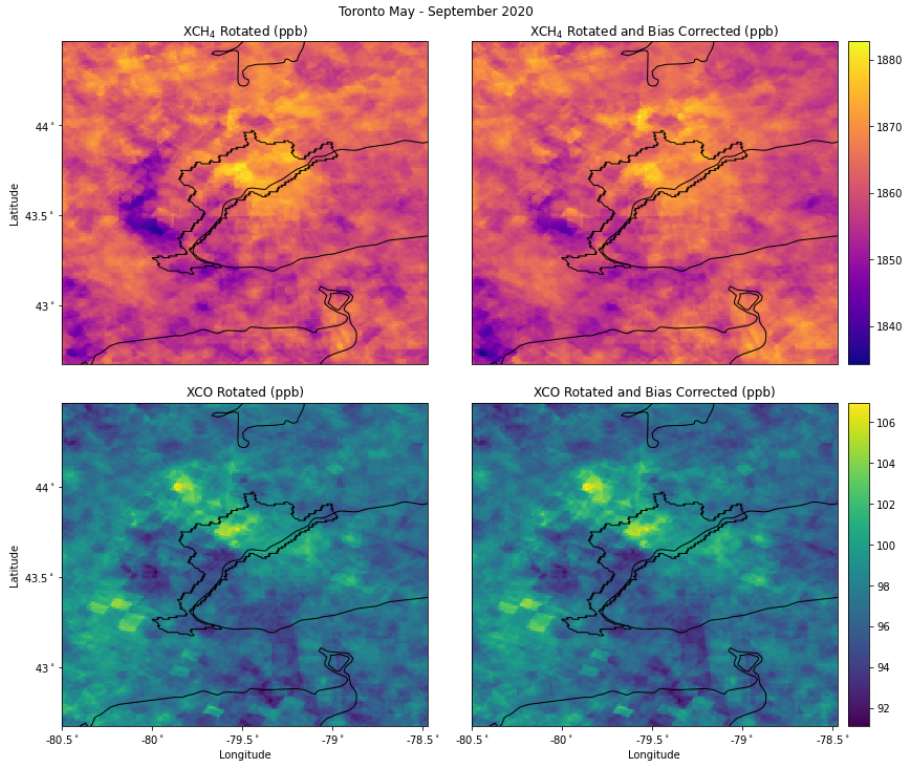


Figure 10: Rotated/oversampled TROPOMI  $\text{CH}_4$  and  $\text{CO}$  omitting (left) and including (right) bias correction.

To calculate anomalies, we subtract the background surface from the oversampled column-averaged dry air mole fraction at every grid cell (bottom right Figure 11). Before we can calculate enhancement ratios, we must divide the oversampled anomalies by the oversampled values of the averaging kernels at the surface (Appendix section A.1). This process accounts for the sensitivities of the column measurements on variations at the surface, where we assume the emissions are happening (Wunch et al., 2009, 2016).

We want to compare the enhancements of the various trace gases, but most of the grid cells in our anomalies scenes form the background. We choose a plume box based on the city centroid, which formed the pivot point for rotation. It extends  $0.2^\circ$  west,  $0.7^\circ$  east, and  $\pm 0.3^\circ$  north-south of the city centroid. This box usually captures most of the oversampled plumes and is big enough to include some background.

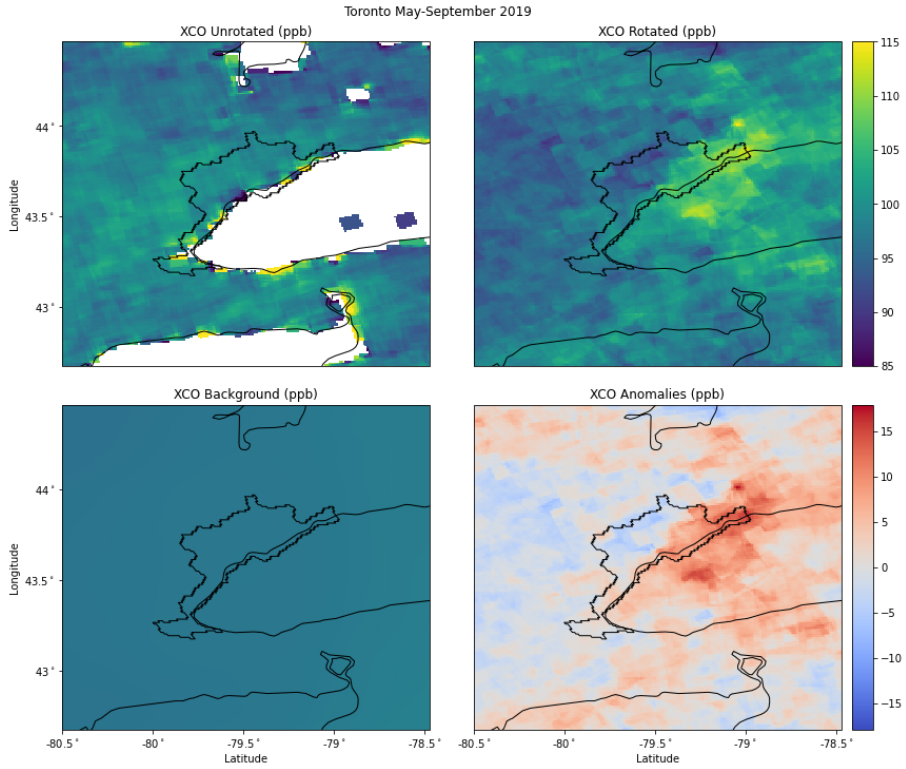


Figure 11: CO anomalies for summer 2019.

To calculate enhancement ratios we regress  $\text{CH}_4$  anomalies onto those of CO and  $\text{NO}_2$  in our plume box. We follow MacDonald et al. (2022) and use a reduced major axis regression (RMA, York et al., 2004), also known as a model 2 regression. This method is used to investigate the underlying relationship between two variables and has the advantage of handling errors in both x and y. On the other hand, OLS specifically probes how one variable affects another. Note that reduced major axis regression will always have a steeper slope than OLS (Smith, 2009).

## 4 Results and Discussion

Table 1 contains the  $\text{CH}_4:\text{CO}$  and  $\text{CH}_4:\text{NO}_2$  enhancement ratios for Toronto from 2018-2021. We determined the  $2-\sigma$  uncertainty estimate by bootstrapping the fit 50 000 times (Efron and Gong, 1983) and taking twice the standard deviation of the fits. We have arranged the results by season because  $\text{CH}_4$  emissions are known to change throughout the year in Toronto. TROPOMI  $\text{NO}_2$  data is only available starting in May 2018, so we do not have values for winter or spring 2018.

Year	Season	CH <sub>4</sub> :CO	Uncertainty	R	Year	Season	CH <sub>4</sub> :NO <sub>2</sub>	Uncertainty	R
2018	DJF	2.35	0.09	0.44	2018	DJF	N/A	N/A	N/A
	MAM	2.36	0.05	0.62		MAM	N/A	N/A	N/A
	JJA	2.31	0.06	0.36		JJA	39.11	1.39	0.09
	SON	2.58	0.05	0.53		SON	89.82	2.12	0.39
2019	DJF	2.13	0.13	0.06	2019	DJF	130.80	247.73	0.00
	MAM	2.07	0.05	0.50		MAM	97.44	2.71	0.43
	JJA	1.20	0.02	0.80		JJA	84.11	2.56	0.15
	SON	2.56	0.05	0.43		SON	42.92	1.08	0.25
2020	DJF	-1.36	0.04	0.22	2020	DJF	89.94	3.01	0.41
	MAM	2.58	0.08	0.69		MAM	97.86	3.30	0.37
	JJA	2.93	0.07	0.38		JJA	78.26	2.31	0.38
	SON	1.65	0.04	0.30		SON	48.59	1.24	0.40
2021	DJF	3.53	0.11	0.29	2021	DJF	149.51	7.26	0.60
	MAM	2.18	0.05	0.54		MAM	53.95	1.08	0.52
	JJA	1.27	0.03	0.31		JJA	103.02	3.39	0.28
	SON	-1.25	0.03	-0.10		SON	61.41	1.43	0.25

Table 1: Toronto Enhancement Ratios.

Note that throughout this work DJF refers to January and February of the listed year, but December of the previous year.

## 4.1 CH<sub>4</sub>:CO

We find the best correlation ( $R=0.80$ ) between CH<sub>4</sub> and CO anomalies in the summer of 2019. Figure 12 shows the rotated and oversampled data for this season and the anomalies in the plume box. It also shows a scatter plot of the grid cells and the RMA regression line that generates the enhancement ratio. For this season we see coincident, well defined plumes and a relatively smooth background. The plume box also nicely captures the CO plume without incorporating too much of the background. We find that coverage is the most important factor for finding good correlation between anomalies. In summer 2019, each grid cell has many satellite pixels contributing to its values. This leads to smoother scenes overall and reduces the influence of individual overpasses.

In general, R values are higher in the spring and summer than in the fall or winter. This is almost certainly due to clouds limiting the number of successful retrievals in the colder months. We can see the consequences of poor coverage in winter 2019 (Appendix section A.2). Many grid cells in the plume box do not overlap with a single satellite pixel leading to data gaps and fewer pixels for the regression. Other grid cells are part of an isolated rectangle, which means all

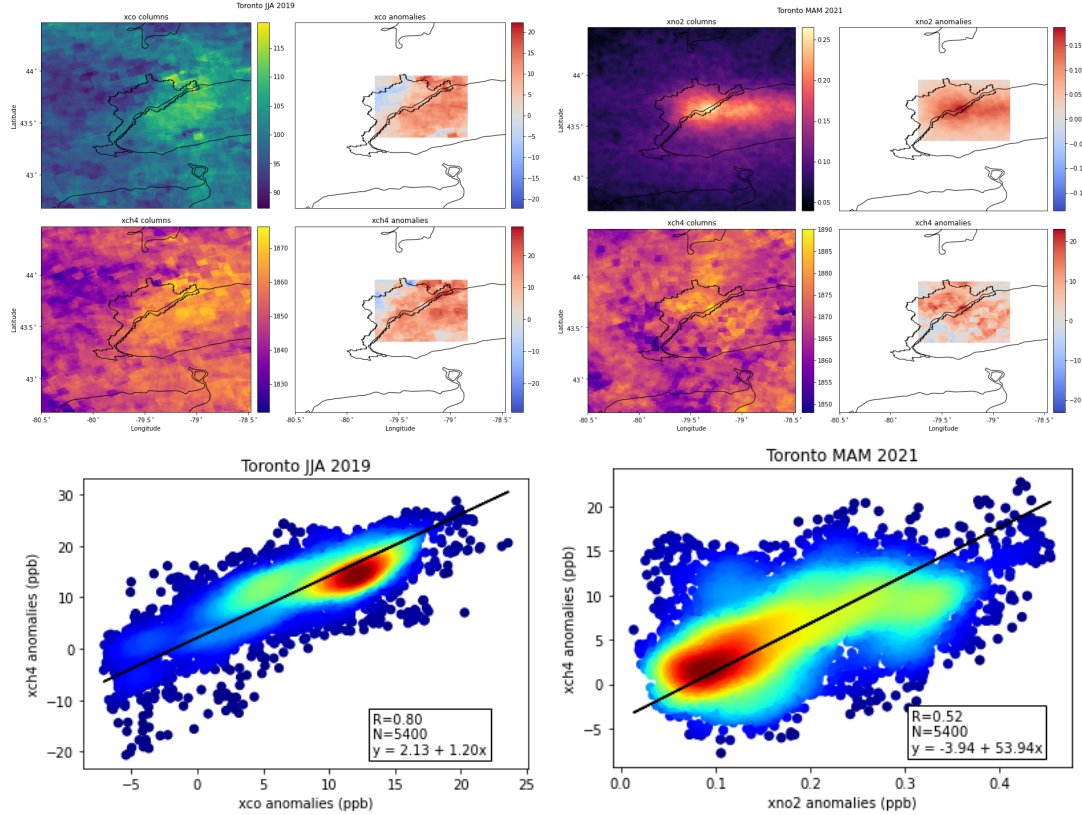


Figure 12: Seasonal enhancement ratios with best correlation coefficient.

of their information comes from a single satellite pixel. The poor coverage does not allow for enough pixel averaging and too few measurements are contributing too much information. Our method may not be suitable for these months and we may need to use a more careful scene by scene analysis (MacDonald et al., 2022; Plant et al., 2022) in the future. Appendix section A.2 shows CH<sub>4</sub> and CO anomalies for the rest of 2019 and 2020.

We have also plotted the enhancement ratio yearly trends for any season with  $R > 0.30$  (Figure 13 left side). In 2018, 2019, and 2021 we see CH<sub>4</sub>:CO at its minimum during the summer months. Natural gas building heating is a significant source of CH<sub>4</sub> in urban areas that is entirely nonexistent in Toronto in the summertime. Other urban sources such as gas stoves and hot water boilers will emit relatively consistently throughout the year. So we would expect CH<sub>4</sub> emissions to be lowest in the summer months. On the other hand, the most significant source of CO emissions in cities is incomplete combustion from cars (EPA, 2008). Studies have shown that people drive more on average in the summer (Triplett et al., 2016), so

we expect CO emissions to be higher. For these two reasons, we expect CH<sub>4</sub>:CO to be lowest in the summer, which matches with our observations. We see the opposite trend in 2020. But this year is exceptional due to the extensive COVID-19 related lockdowns that occurred in Toronto and throughout the world. There has been a great deal of research that investigates reductions in anthropogenic trace gas emissions due to these lockdowns (Laughner et al., 2021; Chen et al., 2022). During the summer of 2020, there were substantially fewer cars on the roads and therefore less CO being emitted in Toronto. This reduction in traffic could account for the higher enhancement ratio we see at this time.

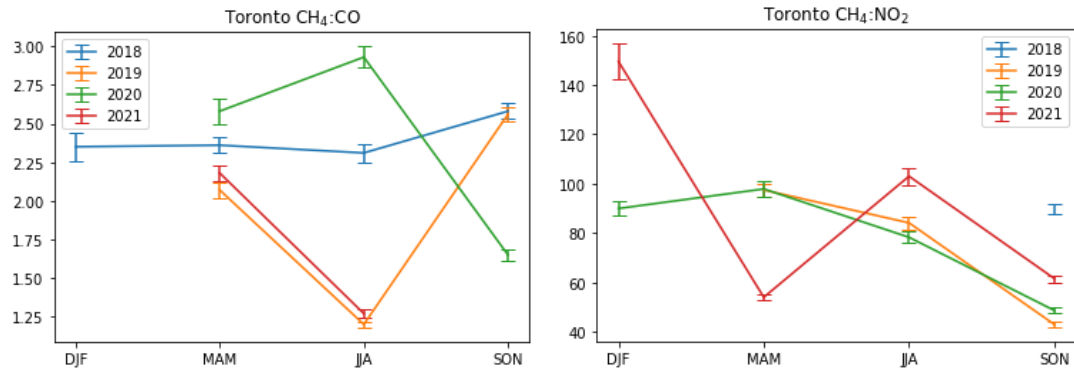


Figure 13: CH<sub>4</sub>:CO and CH<sub>4</sub>:NO<sub>2</sub> annual trends.

## 4.2 CH<sub>4</sub>:NO<sub>2</sub>

We find the best correlation between CH<sub>4</sub> and NO<sub>2</sub> anomalies in the winter of 2021, but this is likely a fluke due to very poor CH<sub>4</sub> coverage and many unpopulated grid cells. Our second best correlation ( $R=0.52$ ) occurred in spring 2021 and is shown on the right side of Figure 12. The rest of 2021 is included in Appendix section A.3. We typically see an intense NO<sub>2</sub> enhancement which smoothly decays in all directions, while the CH<sub>4</sub> enhancement is much more diffuse and noisy. As previously mentioned, an NO<sub>2</sub> enhancement is much more obvious due to three factors: the short lifetime (low background), the smaller pixel size, and the greater coverage. In the oversampled NO<sub>2</sub> scenes, individual satellite pixels are not even visible because of the extensive overlap. This shows the strengths of this method when there is sufficient available data. There is another possible issue in the alignment of the CH<sub>4</sub> and NO<sub>2</sub> plumes that can be seen in summer 2021 (Appendix section A.3) and other figures not included. Sometimes the NO<sub>2</sub> plume does not extend as far as the CH<sub>4</sub> plume and has its most intense point closer to the city centroid. This could be related to the much

shorter lifetime of  $\text{NO}_2$ . If the winds are not blowing very strongly, it is possible that the  $\text{NO}_2$  decays significantly and has a measured plume much shorter than that of  $\text{CH}_4$ . Some papers such as MacDonald et al. (2022) include a correction factor to adjust for this difference.

The right side of Figure 13 shows the yearly trends in  $\text{CH}_4:\text{NO}_2$  enhancement ratios. We use a less restrictive  $R > 0.25$  cutoff because the correlations are worse overall than for  $\text{CH}_4:\text{CO}$ . However we expected the more well-defined  $\text{NO}_2$  enhancements to lead to better correlations. This could indicate that the simultaneous retrieval of  $\text{CH}_4$  and  $\text{CO}$  is leading to higher correlations rather than our method really aligning plumes of different species. It is difficult say anything about the annual trends in  $\text{CH}_4:\text{NO}_2$ . The main source of  $\text{NO}_2$  in urban areas is from combustion of non-methane fossil fuels EPA (2008) and in Toronto vehicles are the largest factor. We do not see as drastic of a change in 2020 like we do for  $\text{CH}_4:\text{CO}$ , but we do see a higher  $\text{CH}_4:\text{NO}_2$  ratio in the summer and fall of 2020 after the start of COVID-19 related lockdowns.

The poorer correlations between  $\text{CH}_4$  and  $\text{NO}_2$  are somewhat alarming. One possible solution would be to reduce the number of ratios we calculate per year. For example we could separate the year into three 4-month pieces or two 6-month pieces. Or we could skew the time window for each ratio, allowing cloudier seasons to be grouped together. We have investigated many of these ideas already and there are promising possibilities, but we have yet to do the in depth analysis required. By grouping more data into the same scene, we will inevitably see less noisy enhancements. For example, Maasakkers et al. (2022) obtained a very distinct methane plume originating from a landfill by incorporating all available data into a single analysis. We have also investigated filtering to some extent, but it is not included in this work. Due to the predominantly westerly winds in Toronto, many  $\text{CH}_4$  overpasses should have plumes over lake Ontario, but those pixels almost never pass quality assurance. So many overpasses do not contribute to the enhancement at all and an argument could be made for their exclusion.

## 5 Future Work

The most important work to be done is to validate this methodology. In Toronto, we can do this with the network of ground-based EM27/SUN spectrometers in the city maintained by Professor Debra Wunch and Environment and Climate Change Canada. These instruments measure column-averaged dry air mole fractions of trace gases like  $\text{CH}_4$ ,  $\text{CO}$ , and  $\text{CO}_2$ , which makes them perfectly suited for validating satellite data products. They are also much more accurate and

precise and measure far more frequently over Toronto than TROPOMI. While there are only a handful of detectors throughout the city, we can still calculate enhancements by considering the winds and carefully selecting the right detector as the background source. We can obtain enhancement ratios and directly compare them to those in this work. This would be a reliable way to know if our method is really capturing reality. We will also expand our analysis to other cities with extensive ground-based instrument networks like Los Angeles and Boston. It is possible that Toronto is difficult to analyze due to the presence of the lake, local weather patterns, and the geometry of the city.

We would also like to incorporate CO<sub>2</sub> data from OCO-2/3, possibly using techniques from MacDonald et al. (2022). The ratios derived with CO<sub>2</sub> would provide more opportunities to validate our technique with ground-based instruments or to compare to existing literature and emission inventories. We also urgently need to add a method for calculating uncertainty. We attempted to copy the process outlined in MacDonald et al. (2022), but it was a severe underestimate of the uncertainty. The authors used 500 iterations of bootstrapping with replacement, but we have thousands of grid cells contributing to the regression rather than hundreds of satellite pixels. We will need to develop another technique, but it will likely be based on bootstrapping which is popular in past research on enhancement ratios.

By the end of 2022, version 2 of the operational TROPOMI CH<sub>4</sub> product (Lorente et al., 2021) will be released. This is set to include updates to spectroscopy, a posteriori bias corrections, and the full-physics retrieval algorithm. Validation against TCCON shows that the CH<sub>4</sub> random error (5.6 ppb/ $\sim$ 0.3%) is significantly less than that of the WFMD product we use here (12.39 ppb/ $\sim$ 0.8%), with similar levels of bias. Research similar to our own has already been published (Maasakkers et al., 2022) using an early edition of this update, so we are hopeful that an analysis with this new dataset will improve some of our results. This will also give us an opportunity to directly compare the operational and WFMD products and gain insight into their differences.

Eventually we would also like to investigate urban emissions with a high-resolution chemistry transport model. We would like to know if methane measurements from TROPOMI have the accuracy, precision, and granularity necessary to be useful on such a small scale. We are also interested in enhancement ratios derived from inventory-driven simulations and how they compare to our results above and those of MacDonald et al. (2022) and Plant et al. (2022). Finally we want to try to assimilate TROPOMI CH<sub>4</sub> observations and see if they contribute to flux inversions of cities like Toronto.

## 6 References

- Akagi, S. K., Yokelson, R. J., Wiedinmyer, C., Alvarado, M. J., Reid, J. S., Karl, T., Crounse, J. D., and Wennberg, P. O. (2011). Emission factors for open and domestic biomass burning for use in atmospheric models. *Atmospheric Chemistry and Physics*, 11(9):4039–4072.
- Altman, N. S. (1992). An Introduction to Kernel and Nearest-Neighbor Non-parametric Regression. *The American Statistician*, 46(3):175–185.
- Chen, J., Jiang, Z., Li, R., Liao, C., Miyazaki, K., and Jones, D. B. A. (2022). Large discrepancy between observed and modeled wintertime tropospheric NO<sub>x</sub> variabilities due to COVID-19 controls in China. *Environmental Research Letters*, 17(3):035007.
- Clarisso, L., Van Damme, M., Clerbaux, C., and Coheur, P.-F. (2019). Tracking down global NH<sub>3</sub> point sources with wind-adjusted superresolution. *Atmospheric Measurement Techniques*, 12(10):5457–5473.
- Crippa, M., Guizzardi, D., Muntean, M., Schaaf, E., Dentener, F., van Aardenne, J. A., Monni, S., Doering, U., Olivier, J. G. J., Pagliari, V., and Janssens-Maenhout, G. (2018). Gridded emissions of air pollutants for the period 1970–2012 within EDGAR v4.3.2. *Earth System Science Data*, 10(4):1987–2013.
- Crisp, D., Atlas, R. M., Breon, F. M., Brown, L. R., Burrows, J. P., Ciais, P., Connor, B. J., Doney, S. C., Fung, I. Y., Jacob, D. J., Miller, C. E., O'Brien, D., Pawson, S., Randerson, J. T., Rayner, P., Salawitch, R. J., Sander, S. P., Sen, B., Stephens, G. L., Tans, P. P., Toon, G. C., Wennberg, P. O., Wofsy, S. C., Yung, Y. L., Kuang, Z., Chudasama, B., Sprague, G., Weiss, B., Pollock, R., Kenyon, D., and Schroll, S. (2004). The Orbiting Carbon Observatory (OCO) mission. *Advances in Space Research*, 34(4):700–709.
- Duren, R. M. and Miller, C. E. (2012). Measuring the carbon emissions of megacities. *Nature Climate Change*, 2(8):560–562.
- Efron, B. and Gong, G. (1983). A Leisurely Look at the Bootstrap, the Jackknife, and Cross-Validation. *The American Statistician*, 37(1):36–48.
- Eldering, A., Taylor, T. E., O'Dell, C. W., and Pavlick, R. (2019). The OCO-3 mission: Measurement objectives and expected performance based on 1 year of simulated data. *Atmospheric Measurement Techniques*, 12(4):2341–2370.

Environment and Climate Change Canada (2022). Canada 2030 Emissions Reduction Plan. *Government of Canada*.

EPA (2008). Latest Findings on National Air Quality. *Office of Air Quality Planning and Standards, Air Quality Assessment Division*.

ESA (2017). Sentinel-5 Precursor Calibration and Validation Plan for the Operational Phase. *European Space Agency*.

Eskes, H., van Geffen, J., Boersma, F., Kai-Uwe, E., Apituley, A., Pedergnana, M., Sneep, M., Veefkind, P., and Loyola, D. (2019). Sentinel-5 precursor/TROPOMI Level 2 Product User Manual Nitrogendioxide. *European Space Agency*.

Eskes, H., van Geffen, J., Sneep, M., Veefkind, P., Sander, N., and Zehner, C. (2021). S5P Nitrogen Dioxide v02.03.01 intermediate reprocessing on the S5P-PAL system: Readme file. *European Space Agency*.

Etminan, M., Myhre, G., Highwood, E. J., and Shine, K. P. (2016). Radiative forcing of carbon dioxide, methane, and nitrous oxide: A significant revision of the methane radiative forcing. *Geophysical Research Letters*, 43(24):12,614–12,623.

Fioletov, V. E., McLinden, C. A., Krotkov, N., Moran, M. D., and Yang, K. (2011). Estimation of SO<sub>2</sub> emissions using OMI retrievals. *Geophysical Research Letters*, 38(21).

Fioletov, V. E., McLinden, C. A., Krotkov, N., Yang, K., Loyola, D. G., Valks, P., Theys, N., Van Roozendael, M., Nowlan, C. R., Chance, K., Liu, X., Lee, C., and Martin, R. V. (2013). Application of OMI, SCIAMACHY, and GOME-2 satellite SO<sub>2</sub> retrievals for detection of large emission sources. *Journal of Geophysical Research: Atmospheres*, 118(19):11,399–11,418.

Florczyk, A., Melchiorri, M., Corbane, C., Schiavina, M., Maffenini, M., Pesaresi, M., Politis, P., Sabo, S., Freire, S., Ehrlich, D., and et al (2019). Description of the GHS Urban Centre Database 2015: Public release 2019 : Version 1.0. *Joint Research Centre, European Comission*.

Gelaro, R., McCarty, W., Suárez, M. J., Todling, R., Molod, A., Takacs, L., Randles, C. A., Darmenov, A., Bosilovich, M. G., Reichle, R., Wargan, K., Coy, L., Cullather, R., Draper, C., Akella, S., Buchard, V., Conaty, A., da Silva, A. M., Gu, W., Kim, G.-K., Koster, R., Lucchesi, R., Merkova, D., Nielsen, J. E., Partyka, G., Pawson, S., Putman, W., Rienerer, M., Schubert, S. D., Sienkiewicz, M., and Zhao, B. (2017). The Modern-Era Retrospective Analysis

for Research and Applications, Version 2 (MERRA-2). *Journal of Climate*, 30(14):5419–5454.

Hachmeister, J., Schneising, O., Buchwitz, M., Lorente, A., Borsdorff, T., Burrows, J. P., Notholt, J., and Buschmann, M. (2022). On the influence of underlying elevation data on Sentinel-5 Precursor satellite methane retrievals over Greenland. *Atmospheric Measurement Techniques Discussions*, pages 1–29.

Hedelius, J. K., Liu, J., Oda, T., Maksyutov, S., Roehl, C. M., Iraci, L. T., Podolske, J. R., Hillyard, P. W., Liang, J., Gurney, K. R., Wunch, D., and Wennberg, P. O. (2018). Southern California megacity CO<sub>2</sub>, CH<sub>4</sub>, and CO flux estimates using ground- and space-based remote sensing and a Lagrangian model. *Atmospheric Chemistry and Physics*, 18(22):16271–16291.

Hu, H., Hasekamp, O., Butz, A., Galli, A., Landgraf, J., Aan de Brugh, J., Borsdorff, T., Scheepmaker, R., and Aben, I. (2016). The operational methane retrieval algorithm for TROPOMI. *Atmospheric Measurement Techniques*, 9(11):5423–5440.

Jacob, D. J. (1999). *Introduction to Atmospheric Chemistry*. Princeton University Press.

Lama, S., Houweling, S., Boersma, K. F., Eskes, H., Aben, I., Denier van der Gon, H. A. C., Krol, M. C., Dolman, H., Borsdorff, T., and Lorente, A. (2020). Quantifying burning efficiency in megacities using the NO<sub>2</sub>/CO ratio from the Tropospheric Monitoring Instrument (TROPOMI). *Atmospheric Chemistry and Physics*, 20(17):10295–10310.

Landgraf, J., aan de Brugh, J., Scheepmaker, R., Borsdorff, T., Hu, H., Houweling, S., Butz, A., Aben, I., and Hasekamp, O. (2016). Carbon monoxide total column retrievals from TROPOMI shortwave infrared measurements. *Atmospheric Measurement Techniques*, 9(10):4955–4975.

Laughner, J. L., Neu, J. L., Schimel, D., Wennberg, P. O., Barsanti, K., Bowman, K. W., Chatterjee, A., Croes, B. E., Fitzmaurice, H. L., Henze, D. K., Kim, J., Kort, E. A., Liu, Z., Miyazaki, K., Turner, A. J., Anenberg, S., Avise, J., Cao, H., Crisp, D., de Gouw, J., Eldering, A., Fyfe, J. C., Goldberg, D. L., Gurney, K. R., Hasheminassab, S., Hopkins, F., Ivey, C. E., Jones, D. B. A., Liu, J., Lovenduski, N. S., Martin, R. V., McKinley, G. A., Ott, L., Poulter, B., Ru, M., Sander, S. P., Swart, N., Yung, Y. L., and Zeng, Z.-C. (2021). Societal shifts due to COVID-19 reveal large-scale complexities and feedbacks between atmospheric chemistry and climate change. *Proceedings of the National Academy of Sciences*, 118(46):e2109481118.

- Lorente, A., Borsdorff, T., Butz, A., Hasekamp, O., aan de Brugh, J., Schneider, A., Wu, L., Hase, F., Kivi, R., Wunch, D., Pollard, D. F., Shiomi, K., Deutscher, N. M., Velazco, V. A., Roehl, C. M., Wennberg, P. O., Warneke, T., and Landgraf, J. (2021). Methane retrieved from TROPOMI: Improvement of the data product and validation of the first 2 years of measurements. *Atmospheric Measurement Techniques*, 14(1):665–684.
- Maasakkers, J. D., Varon, D. J., Elfarsdóttir, A., McKeever, J., Jervis, D., Mahapatra, G., Pandey, S., Lorente, A., Borsdorff, T., Foorthuis, L. R., Schuit, B. J., Tol, P., van Kempen, T. A., van Hees, R., and Aben, I. (2022). Using satellites to uncover large methane emissions from landfills. *Science Advances*, 8(32):eabn9683.
- MacDonald, C. G., Laughner, J. L., Hedelius, J. K., Nassar, R., Mastrogiacomo, J.-P., and Wunch, D. (2022). Estimating Enhancement Ratios of Nitrogen Dioxide, Carbon Monoxide, and Carbon Dioxide using Satellite Observations. *Atmospheric Chemistry and Physics Discussions*, pages 1–30.
- McLinden, C. A., Fioletov, V., Boersma, K. F., Krotkov, N., Sioris, C. E., Veefkind, J. P., and Yang, K. (2012). Air quality over the Canadian oil sands: A first assessment using satellite observations. *Geophysical Research Letters*, 39(4).
- Mostafavi Pak, N., Heerah, S., Zhang, J., Chan, E., Worthy, D., Vogel, F., and Wunch, D. (2021). The Facility Level and Area Methane Emissions inventory for the Greater Toronto Area (FLAME-GTA). *Atmospheric Environment*, 252:118319.
- Nassar, R., Hill, T. G., McLinden, C. A., Wunch, D., Jones, D. B. A., and Crisp, D. (2017). Quantifying CO<sub>2</sub> Emissions From Individual Power Plants From Space. *Geophysical Research Letters*, 44(19):10,045–10,053.
- Nassar, R., Mastrogiacomo, J.-P., Bateman-Hemphill, W., McCracken, C., Macdonald, C. G., Hill, T., O'Dell, C. W., Kiel, M., and Crisp, D. (2021). Advances in quantifying power plant CO<sub>2</sub> emissions with OCO-2. *Remote Sensing of Environment*, 264:112579.
- Pasquill, F. (1961). The estimation of the dispersion of windborne material. *Meteorol. Mag.*, 90:33–49.
- Plant, G., Kort, E. A., Floerchinger, C., Gvakharia, A., Vimont, I., and Sweeney, C. (2019). Large Fugitive Methane Emissions From Urban Centers Along the U.S. East Coast. *Geophysical Research Letters*, 46(14):8500–8507.

- Plant, G., Kort, E. A., Murray, L. T., Maasakkers, J. D., and Aben, I. (2022). Evaluating urban methane emissions from space using TROPOMI methane and carbon monoxide observations. *Remote Sensing of Environment*, 268:112756.
- Pommier, M., McLinden, C. A., and Deeter, M. (2013). Relative changes in CO emissions over megacities based on observations from space. *Geophysical Research Letters*, 40(14):3766–3771.
- Reuter, M., Buchwitz, M., Schneising, O., Krautwurst, S., O'Dell, C. W., Richter, A., Bovensmann, H., and Burrows, J. P. (2019). Towards monitoring localized CO<sub>2</sub> emissions from space: Co-located regional CO<sub>2</sub> and NO<sub>2</sub> enhancements observed by the OCO-2 and S5P satellites. *Atmospheric Chemistry and Physics*, 19(14):9371–9383.
- Saunois, M., Stavert, A. R., Poulter, B., Bousquet, P., Canadell, J. G., Jackson, R. B., Raymond, P. A., Dlugokencky, E. J., Houweling, S., Patra, P. K., Ciais, P., Arora, V. K., Bastviken, D., Bergamaschi, P., Blake, D. R., Brailsford, G., Bruhwiler, L., Carlson, K. M., Carroll, M., Castaldi, S., Chandra, N., Crevoisier, C., Crill, P. M., Covey, K., Curry, C. L., Etiope, G., Frankenberg, C., Gedney, N., Hegglin, M. I., Höglund-Isaksson, L., Hugelius, G., Ishizawa, M., Ito, A., Janssens-Maenhout, G., Jensen, K. M., Joos, F., Kleinen, T., Krummel, P. B., Langenfelds, R. L., Laruelle, G. G., Liu, L., Machida, T., Maksyutov, S., McDonald, K. C., McNorton, J., Miller, P. A., Melton, J. R., Morino, I., Müller, J., Murguia-Flores, F., Naik, V., Niwa, Y., Noce, S., O'Doherty, S., Parker, R. J., Peng, C., Peng, S., Peters, G. P., Prigent, C., Prinn, R., Ramonet, M., Regnier, P., Riley, W. J., Rosentreter, J. A., Segers, A., Simpson, I. J., Shi, H., Smith, S. J., Steele, L. P., Thornton, B. F., Tian, H., Tohjima, Y., Tubiello, F. N., Tsuruta, A., Viovy, N., Voulgarakis, A., Weber, T. S., van Weele, M., van der Werf, G. R., Weiss, R. F., Worthy, D., Wunch, D., Yin, Y., Yoshida, Y., Zhang, W., Zhang, Z., Zhao, Y., Zheng, B., Zhu, Q., Zhu, Q., and Zhuang, Q. (2020). The Global Methane Budget 2000–2017. *Earth System Science Data*, 12(3):1561–1623.
- Schneising, O. (2022). TROPOMI WFM-DOAS XCH<sub>4</sub> -Algorithm Theoretical Basis Document. *ESA Climate Change Initiative "PLUS" (CCI+)*, page 31.
- Schneising, O., Buchwitz, M., Reuter, M., Bovensmann, H., Burrows, J. P., Borsdorff, T., Deutscher, N. M., Feist, D. G., Griffith, D. W. T., Hase, F., Hermans, C., Iraci, L. T., Kivi, R., Landgraf, J., Morino, I., Notholt, J., Petri, C., Pollard, D. F., Roche, S., Shiomi, K., Strong, K., Sussmann, R., Velazco, V. A., Warneke, T., and Wunch, D. (2019). A scientific algorithm to simultaneously retrieve carbon monoxide and methane from TROPOMI onboard Sentinel-5 Precursor. *Atmospheric Measurement Techniques*, 12(12):6771–6802.

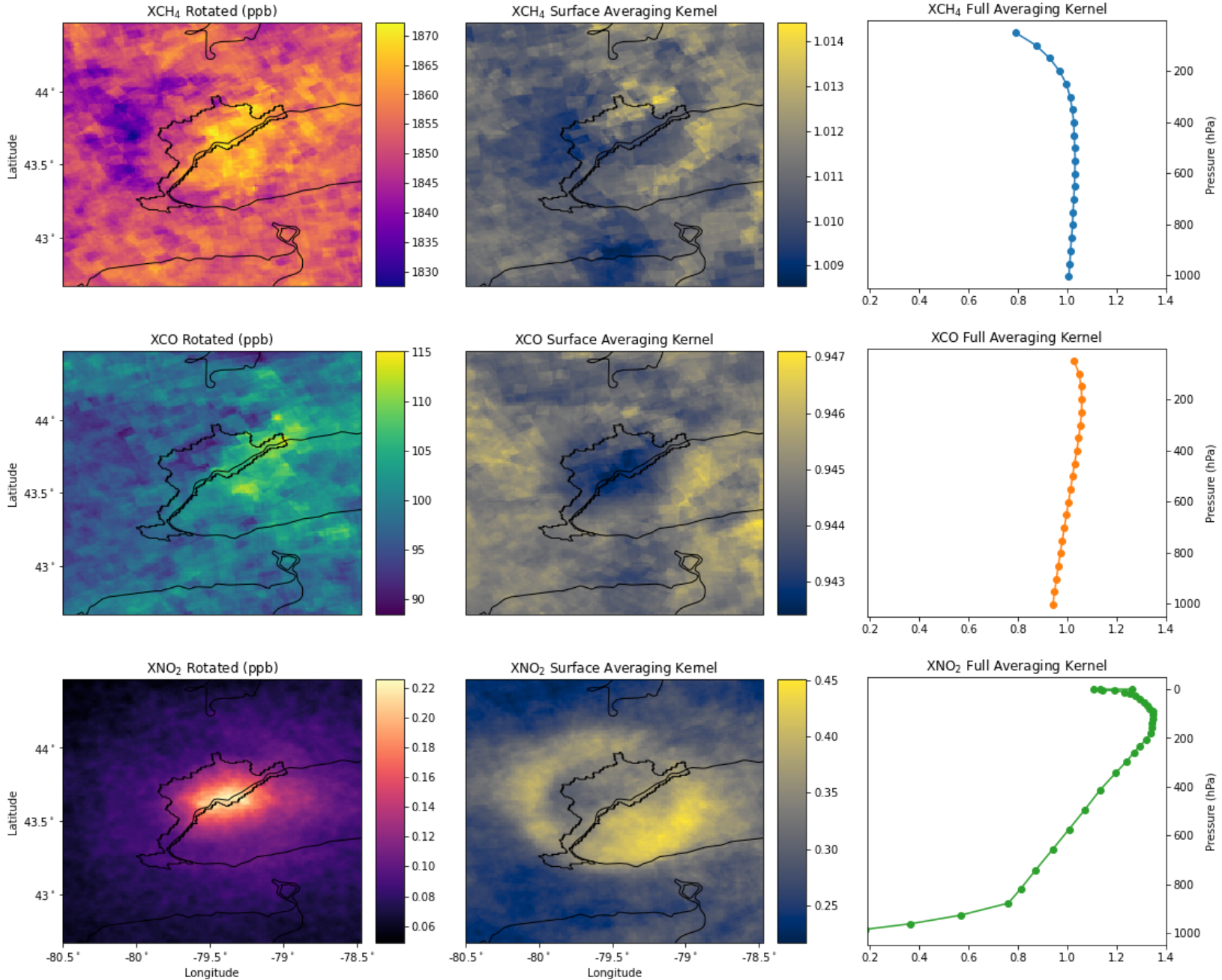
- Smith, R. J. (2009). Use and misuse of the reduced major axis for line-fitting. *American Journal of Physical Anthropology*, 140(3):476–486.
- Sun, K., Zhu, L., Cady-Pereira, K., Chan Miller, C., Chance, K., Clarisse, L., Cocheur, P.-F., González Abad, G., Huang, G., Liu, X., Van Damme, M., Yang, K., and Zondlo, M. (2018). A physics-based approach to oversample multi-satellite, multispecies observations to a common grid. *Atmospheric Measurement Techniques*, 11(12):6679–6701.
- Triplet, T., Santos, R., Rosenbloom, S., and Tefft, B. (2016). American Driving Survey: 2014 – 2015. *AAA Foundation for Traffic Safety*.
- van Geffen, J., Boersma, K. F., Eskes, H., Sneep, M., ter Linden, M., Zara, M., and Veefkind, J. P. (2020). S5P TROPOMI NO<sub>2</sub> slant column retrieval: Method, stability, uncertainties and comparisons with OMI. *Atmospheric Measurement Techniques*, 13(3):1315–1335.
- Veefkind, J. P., Aben, I., McMullan, K., Förster, H., de Vries, J., Otter, G., Claas, J., Eskes, H. J., de Haan, J. F., Kleipool, Q., van Weele, M., Hasekamp, O., Hoogeveen, R., Landgraf, J., Snel, R., Tol, P., Ingmann, P., Voors, R., Kruizinga, B., Vink, R., Visser, H., and Levelt, P. F. (2012). TROPOMI on the ESA Sentinel-5 Precursor: A GMES mission for global observations of the atmospheric composition for climate, air quality and ozone layer applications. *Remote Sensing of Environment*, 120:70–83.
- Wunch, D., Toon, G. C., Hedelius, J. K., Vizenor, N., Roehl, C. M., Saad, K. M., Blavier, J.-F. L., Blake, D. R., and Wennberg, P. O. (2016). Quantifying the loss of processed natural gas within California’s South Coast Air Basin using long-term measurements of ethane and methane. *Atmospheric Chemistry and Physics*, 16(22):14091–14105.
- Wunch, D., Wennberg, P. O., Toon, G. C., Keppel-Aleks, G., and Yavin, Y. G. (2009). Emissions of greenhouse gases from a North American megacity. *Geophysical Research Letters*, 36(15).
- York, D., Evensen, N. M., Martínez, M. L., and De Basabe Delgado, J. (2004). Unified equations for the slope, intercept, and standard errors of the best straight line. *American Journal of Physics*, 72(3):367–375.
- Zheng, T., Nassar, R., and Baxter, M. (2019). Estimating power plant CO<sub>2</sub> emission using OCO-2 XCO<sub>2</sub> and high resolution WRF-Chem simulations. *Environmental Research Letters*, 14(8):085001.

Zhu, L., Jacob, D. J., Keutsch, F. N., Mickley, L. J., Scheffe, R., Strum, M., González Abad, G., Chance, K., Yang, K., Rappenglück, B., Millet, D. B., Baasandorj, M., Jaeglé, L., and Shah, V. (2017). Formaldehyde (HCHO) As a Hazardous Air Pollutant: Mapping Surface Air Concentrations from Satellite and Inferring Cancer Risks in the United States. *Environmental Science & Technology*, 51(10):5650–5657.

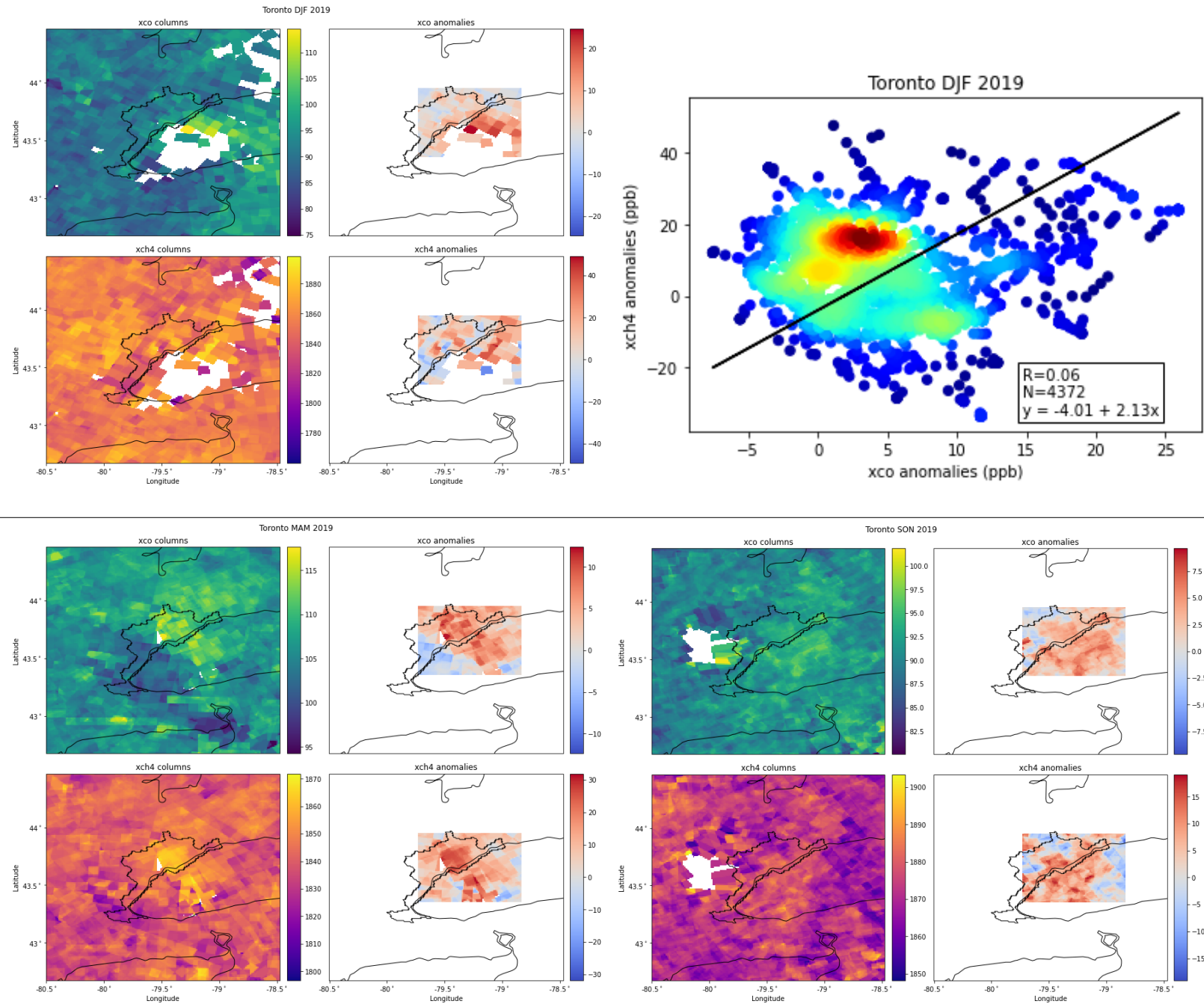
# A Appendix

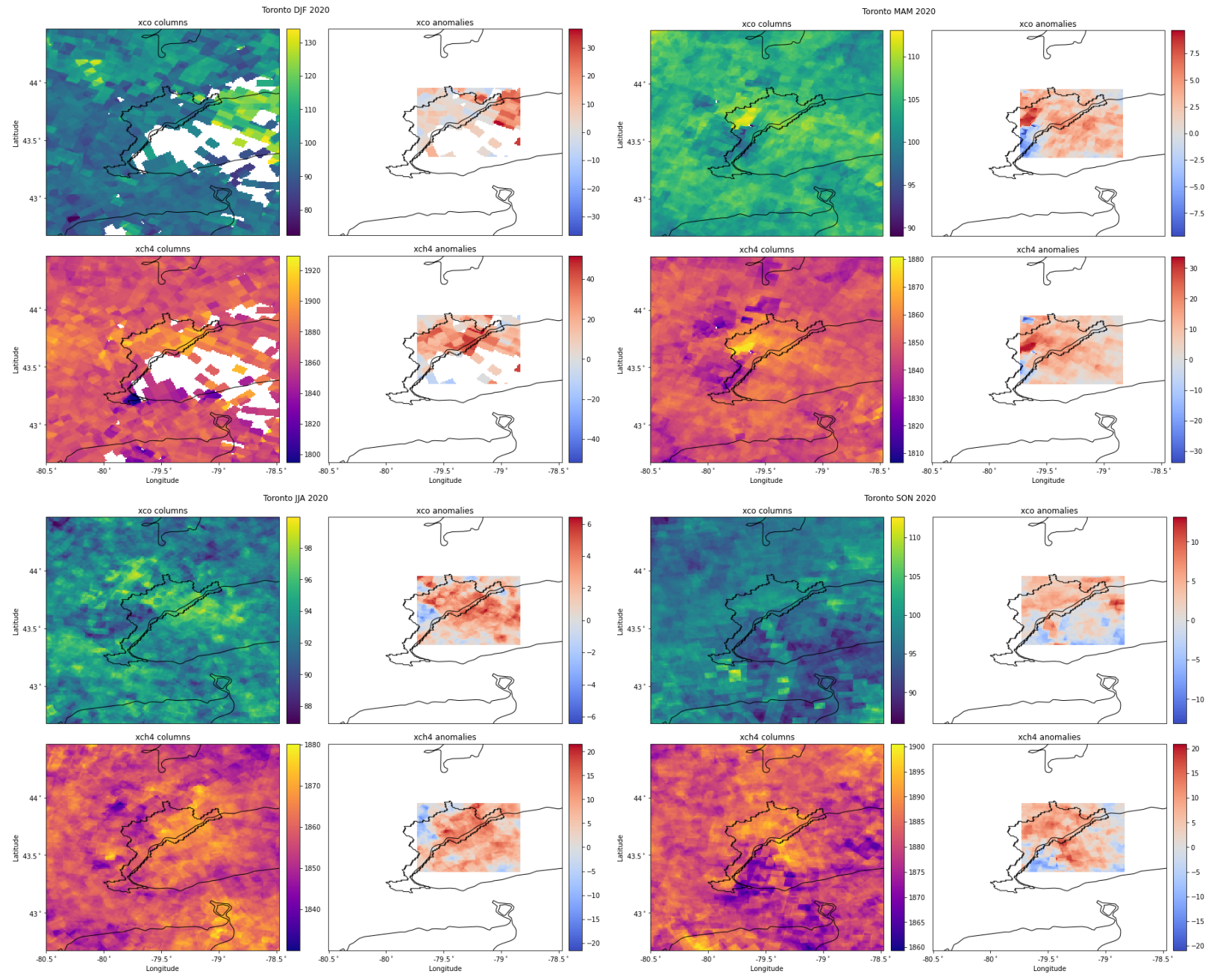
## A.1 Averaging Kernels

Toronto May-September 2019



## A.2 CH<sub>4</sub>:CO Examples





### A.3 CH<sub>4</sub>:NO<sub>2</sub> Examples

